Predicting how lipid composition controls protein curvature sensing with a continuum bilayer membrane model

Yiben Fu[1], David Johnson[2], Andrew Beaven[3], Alexander Sodt[3], Wade Zeno[2], Margaret Johnson[1]

[1]*T. C. Jenkins Department of Biophysics, The Johns Hopkins University, 3400 N. Charles St., Baltimore, Maryland 21218, USA*

[2]*Mork Family Department of Chemical Engineering and Materials Science, The University of Southern California, Los Angeles, California, 90089, USA*

[3]*Eunice Kennedy Shriver National Institute of Child Health and Human Development, National Institutes of Health, 9000 Rockville Pike, Bethesda, Maryland 20892, USA*

Abstract

For a variety of biological processes including endocytosis and signaling, proteins must recruit from the cytoplasm to membranes. Several membrane-binding proteins recognize not only the chemical structure of the membrane lipids but the curvature of the surface, binding more strongly to more highly curved surfaces. One common mechanism of curvature sensing is through the insertion of an amphipathic helix into the outer membrane leaflet. Because lipid composition affects multiple material properties of the membrane including bending rigidity, thickness, lipid tilt, and compressibility, it has not been possible to predict how lipid composition controls protein curvature sensing by helix insertion. Here we develop and apply a two-leaflet continuum membrane model to quantify how such changes to the material properties can favor or disfavor protein curvature sensing by computing energetic and structural changes upon helix insertion, with corroboration against *in vitro* experiments. Our membrane model builds on previous work from our group to explicitly model both monolayers of the bilayer via representation by continuous triangular meshes. To the energy of each monolayer, we introduce a coupling energy that is derived from established energetics of lipid tilt but reformulated into a height term that is methodologically simpler to evaluate. In agreement with molecular dynamics simulations, our model produces a decrease in bilayer height around the site of insertion. We find that increasing membrane height increases curvature sensing. From the protein perspective, deeper or larger insertions also increase curvature sensing. Our experiments of helix insertion by the epsin N-terminal homology (ENTH) on vesicles with varying lipid tail groups show that lipids like DOPC drive stronger curvature sensing than DLPC, despite having the same head-group chemistry, confirming how the material properties of the membrane alter curvature sensing, in excellent agreement with the predictions of our bilayer membrane model. Our model thus quantitatively predicts how changes to membrane composition can alter membrane energetics driven by protein insertion, and can be more broadly extended to characterizing the structure and energetics of protein-driven membrane reshaping by protein assemblies.

Introduction

Cytoplasmic proteins that bind biological membranes are essential for membrane remodeling pathways like clathrin-mediated endocytosis [1, 2] and cell division [3]. Protein domains that mediate membrane binding are often classified by their recognition of specific lipid head groups such as for PI(4,5)P_2 binding. However, experimental studies have shown how multiple membrane binding domains can also recognize membrane curvature, including the epsin N-terminal homology (ENTH) domain, the bin-amphiphysin-rvs (BAR) domain [4], and septins[3]. For the ENTH domain, this curvature 'sensing' ability stems from its N-terminal amphipathic helix, which inserts into the outer leaflet of the bilayer, generating asymmetry between the top and bottom leaflet[5, 6]. Helix inserting domains like ENTH bind more strongly to more highly curved vesicles, and truncation of this helix effectively eliminates the curvature sensing ability[5]. These amphipathic, membrane-inserting helices are common to a variety of membrane binding proteins (septins, arfGAP, amphiphysin), but they do not all exhibit the same curvature sensing abilities across experimental conditions. While this can in part stem from differences in the sequence or length of the helices[7], the composition of the membrane also plays a role, as the insertion of the helix will locally perturb the membrane. Because changing the membrane lipid composition will influence multiple material properties of the membrane, including bending rigidity, thickness, and compressibility, it has not been possible to quantify how lipid composition impacts curvature sensing. Here we use a continuum membrane model that accounts for these material properties of the membrane to perform a quantitative analysis of curvature sensing with validation against new *in vitro* experiments using the ENTH domain.

Computation and theory provide highly controlled and tunable methods to quantify the energetic and structural changes arising from helix insertion in membrane bilayers. However, tradeoffs in capturing molecular detail vs micron-scale membrane surfaces have thus far limited a quantitative comparison of lipid composition and membrane thickness on curvature sensing. At the molecular scale, molecular dynamics (MD) simulations have measured the distribution of membrane stress due to helix insertion [8] and shown how defects in the local ordering of the lipid membrane can regulate helix insertion [9, 10] on flat membranes. On curved membranes, MD simulations characterized how helix insertions can orient along the membrane axis with lower curvature[11], and can radially alter local lipid order [12]. Computational expense limits MD to the nanometer scale, preventing characterization at a range of curvature. Classic elasticity theory

allows a range of elastic moduli for evaluating solid-like deformations along the membrane thickness axis, applicable to nearly arbitrary lengthscales [13] while modeling the large *local* stresses resulting from helix insertion [14]. Previous work employed an efficient two-dimensional model, translationally invariant along a cylindrical axis, that could not account for the anisotropic membrane deformation around a finite helix. Continuum *surface* models that we use here (e.g., Helfrich-Canham-Evans, or HCE[15-17]) sit at an intermediate or mesoscale resolution that is computationally much more efficient than MD simulations and more flexible than classical elasticity theory-based continuum models. While they lack the single-lipid resolution of molecular approaches, they can simultaneously measure energetic and structural changes of membranes in response to a range of perturbations at the micron scale [7, 18]. By representing the surface in 3D space using points on a 2D triangular mesh, these models can capture realistic membrane shapes with arbitrary topologies[18].

In recent work we implemented such a thin-film continuum surface model that successfully predicted curvature sensing by helix insertion with excellent agreement to experiment, further quantifying how bending rigidity and helix size influenced curvature sensing [7]. However, this single-layer membrane lacks internal membrane structure, offering no way to vary the thickness of the bilayer or independently modulate the properties of the inner and outer leaflet. As a result, it has not been possible to evaluate how lipid composition and its material properties or asymmetry across the two leaflets alters curvature sensing, despite its significance in biological membranes [19]. For example, the plasma membrane is known to be actively maintained with a highly asymmetric composition, resulting in distinct curvature preferences and bending rigidities for the two leaflets [20]. Further, lipids with different tail groups are measured to have distinct tilt moduli [21], which influences membrane thickness and how it responds to perturbation. Transmembrane proteins have a thickness that influences their partitioning within membranes of complex compositions, preferring to match their thickness to similarly sized bilayers to minimize their energy. We therefore developed here a double-layer continuum surface model that addresses these limitations of the single-layer model (Fig 1), capturing distinctions between the two leaflets and the role of membrane thickness in membrane structure and energetics.

A key development for the double-leaflet continuum model is to incorporate the coupling between the two leaflets. Variations between leaflets can be modeled at a range of resolution. The curvature-inducing effect of differential stress[22] on an HCE surface can be captured with the

area-difference elasticity (ADE) model [23, 24]. However, the ADE model assumes a uniform membrane thickness throughout the surface [23], and thus cannot model local thickness changes induced by helix insertions. Alternatively, a dual-leaflet Helfrich model with the so-called *Monge* representation can be formulated to describe thickness [25-28]. However, this formulation is only applicable for relatively small deformations; it cannot account for the highly localized deformation underneath the helix. Elasticity theory (see for example Ref [29]) resolves three dimensional structural changes, with local elastic constants that fully determine the bending, area/thickness, and tilt moduli of a tilt-augmented HCE model [30-33]. In this extended HCE model [30-33], lipid orientations must be defined as vectors from the lipid tail to the lipid head. This requires a fixed definition of the start and end mesh points for a specific lipid to be able to calculate its tilt. We find a more flexible option is to reformulate this tilt energy by its impact on membrane height, or the distance between the two leaflets. We use the term height to indicate tilt, and to differentiate from thickness which is coupled to area. To elaborate, an important consideration is ensuring that membrane shape changes influencing area, curvature, and thickness are not 'double-counted' within the energy function. In particular, if the membrane is assumed to be incompressible, then the lateral stretching of the membrane area is equivalent to the vertical reduction in membrane thickness, and thus both thickness and area changes do not contribute independently to the membrane energy. We retain this assumption in our model. The tilt energy, however, is always evaluated independently of the area energy, and by converting tilt modulus into a height modulus, we retain two independent contributions to the energy but in the form of both an area and a height (rather than tilt) term.

In this paper, we first describe our theoretical derivation of the coupled two-leaflet energy function based off of the area-difference-elasticity model [23, 24] and the tilt-curvature augmented Helfrich model [30-32], with the purpose of relaxing the uniform thickness approximation by adding in the tilt energy. In our derivation, we define a membrane height elasticity that is decoupled from the membrane area elasticity. Our height modulus derives from the tilt modulus. Our numerical implementation of the membrane surface builds from our one-layer surface [7, 34] to introduce an outer mesh layer, an inner mesh layer, and the interface layer between the two monolayers, allowing for variations in the local leaflet height/tilt and material properties of each leaflet. We use feedback from MD simulations to validate the local height change introduced to the membrane by the helix insertion. With this model, we then characterize how changes to the

membrane height, tilt modulus, bending modulus, leaflet spontaneous curvature, leaflet asymmetry, and helix size quantitatively alter curvature sensing on vesicles of varying curvature. We performed *in vitro* experiments on vesicles with the same lipid head-group chemistry but varying tail groups, contrasting DOPC, DLPC, and DPPC. Using literature values for the material properties of these membranes, our model can predict how the strength of curvature sensing changes with lipid composition, in excellent agreement with the experiments. We discuss how our model provides a resource for predicting the energetics of protein-driven membrane remodeling, and our results provide a foundation for predicting how distinct membranes will impact protein recruitment as key material properties are varied.

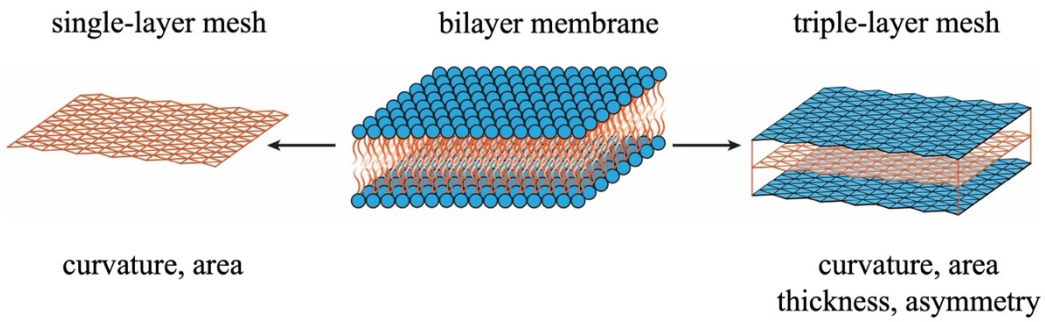

Figure 1. The continuum membrane model is extended here to capture both leaflets of the membrane bilayer. In the middle panel, we illustrate a bilayer membrane consists of two lipid monolayers, with tail groups in orange and head groups in blue. The left panel shows a continuum membrane model using a single-layer triangular mesh, which represents the mid-surface of the bilayer membrane. This model accurately captures changes in membrane curvature and area elasticity. The right panel shows the new continuum membrane model with a triple-layer of triangular meshes. This new model simulates both monolayers simultaneously, allowing for the analysis of curvature changes and area elasticity in each monolayer, as well as the deformation of the leaflet height due to lipid tilt, and asymmetry in leaflet properties.

Theory of the bilayer membrane energy

1. Background on expression for bilayer membrane energy

Lipid bilayers are composed of two lipid monolayers or leaflets in contact via their hydrophobic tails. The energy of the bilayer membrane can be defined by the sum of the individual mechanical energies of the each monolayers, an energy due to the geometrical constraint between the two monolayers [23], and any external work on the system. We thus define the total energy of the system as:

$$E = \sum_{i=1}^{2} E_i + E_h + E_V, \tag{1}$$

where E_i is the monolayer energy, and the index i = 1, 2 refers to the inner and outer monolayer, respectively. E_h is the energy describing the coupling between the two monolayers which will be discussed below. For the enclosed membrane, like the vesicle membrane, the energy term E_V is incorporated to represent the restriction on the volume enclosed by the membrane,

$$E_V = \frac{1}{2}\mu_V \frac{(V - V_0)^2}{V_0}, \tag{2}$$

where μ_V is the coefficient of the volume constraint, and V_0 is the equilibrium or target volume. The volume constraint is an equivalent description of the difference between the osmotic pressures inside and outside the vesicle [35]. Previous work found the volume constraint contributes minimally to the overall energetics given the stable difference between the osmotic pressure inside and outside the vesicle, even when perturbed by α-helix insertion [7]. For unenclosed or infinite membranes, such as cylindrical and planar membranes, there is no volume constraint or E_V term. The mechanical energy of the monolayer is given as the HCE Hamiltonian [15, 16, 23],

$$E_i = \int \frac{1}{2}\kappa_i \left(2c_i - c_{0,i}\right)^2 dA_{0,i} + \frac{1}{2}\mu_{A,i} \frac{\left(A_i - A_{0,i}\right)^2}{A_{0,i}}, \tag{3}$$

where κ_i is the bending modulus, c_i is the mean curvature evaluated at each position on the surface, $c_{0,i}$ is the spontaneous curvature, $\mu_{A,i}$ is the area elasticity modulus, A_i is the area and $A_{0,i}$ is the equilibrium area. As above, the index i = 1, 2 refers to the inner monolayer and outer monolayer, respectively. For simplicity, the two monolayers have the same lipid compositions and thus the same physical properties, *i.e.* $\kappa_1 = \kappa_2$, $\mu_{A,1} = \mu_{A,2}$, and $c_{0,1} = -c_{0,2}$ where the minus represents

that the two monolayers have opposite lipid orientation. Constants κ, μ_A, c_0 represent the single leaflet (mono bending modulus, area elasticity modulus and spontaneous curvature, respectively).

2. Derivation of the monolayer equilibrium area

Values of parameters in Eq (3), namely κ, μ_A and c_0, only rely on the lipid composition and can be directly obtained from prior experimental data. However, the parameter, $A_{0,i}$, cannot be directly determined through prior experiments. In this analysis, we establish a relationship between $A_{0,i}$, the lipid composition, and the membrane geometry. Consider a bilayer membrane with monolayer height h, and a mid-surface with area A_m. Without external force, a flat membrane will reach equilibrium and its two monolayers will have equal areas, *i.e.* $A_i = A_{0,i} = A_m$. For a curved membrane, such as spherical or cylindrical membrane, we suppose it is generated in two steps. First, the flat membrane is bent into a curved shape with A_m fixed and the membrane height unchanged. Second, to relax the membrane compression on the inner layer and stretching on the outer layer due to their distinct radii, lipids flip from the inner monolayer to the outer monolayer [36]. We assume lipid flipping does not influence the membrane size A_m or the membrane height, but results in the decrease of the equilibrium area of the inner monolayer and increase of the equilibrium area of the outer monolayer. We introduce γ as the ratio of the number of inner lipids flipped to the outer monolayer relative to the total number of inner lipids. The equilibrium area of the inner monolayer and the outer monolayer can be expressed as

$$\begin{cases} A_{0,1} = (1-\gamma)A_m \\ A_{0,2} = (1+\gamma)A_m \end{cases}, \tag{4}$$

Note the sum of the equilibrium areas of the two monolayers is independent of γ, $A_{0,1} + A_{0,2} = 2A_m$, preserving mass conservation.

For a regularly shaped membrane like the sphere or cylinder, the curvature is uniform on the surface. The sum of the energy of the two monolayers is now

$$E_{1+2} = \frac{1}{2}\kappa(2c_1 - c_0)^2 A_{0,1} + \frac{1}{2}\mu_A \frac{\left(A_1 - A_{0,1}\right)^2}{A_{0,1}} + \frac{1}{2}\kappa(2c_2 + c_0)^2 A_{0,2} + \frac{1}{2}\mu_A \frac{\left(A_2 - A_{0,2}\right)^2}{A_{0,2}}, \tag{5}$$

where we assumed both leaflets have the same material properties (κ, μ_A and c_0). After relaxation due to lipid flipping, the curved membrane relaxes to the equilibrium state. The value of γ can be determined by minimizing the membrane energy,

$$\frac{\partial E_{1+2}}{\partial \gamma} = 0 \tag{6}$$

to therefore define $A_{0,1}$ and $A_{0,2}$ via Eq. 4. The specific expression for γ depends on the membrane geometry. In the following sections, we will derive the expression for γ in the case of spherical, cylindrical, and planar membrane, respectively.

2.1 Spherical membrane

For a spherical vesicle formed by this membrane, the sphere radius R is defined by the radius of the mid-surface, whose area is $A_m = 4\pi R^2$. The area of the inner monolayer is $A_1 = 4\pi(R-h)^2$ and the area of the outer monolayer is $A_2 = 4\pi(R+h)^2$. The mean curvature of the inner monolayer is $c_1 = 1/(R-h)$ and of the outer monolayer is $c_2 = 1/(R+h)$. By inserting these into Eq. 5 along with Eq. 4, Eq. 6 then produces the expression:

$$\frac{(R-h)^4}{R^4(1-\gamma)^2} - \frac{(R+h)^4}{R^4(1+\gamma)^2} = \frac{\kappa}{\mu_A}\left[\left(\frac{2}{R-h} - c_0\right)^2 - \left(\frac{2}{R+h} + c_0\right)^2\right] \tag{7}$$

Eq (7) shows that γ is dependent on the vesicle size R, the monolayer height h, lipid spontaneous curvature c_0, bending modulus κ and area elasticity modulus μ_A. The analytical expression of γ can be found by the general formula for finding the roots to quartic equations [37] or by numerical methods. This result simplifies if the right-hand side of Eq (7) equals to 0, which is satisfied for two situations: (i) The monolayer has $c_0 = 2h/(R^2 - h^2)$; (ii) The vesicle is large. Then we have

$$\gamma = \frac{2Rh}{R^2 + h^2} \tag{8}$$

Now, γ is only dependent on the vesicle size R and the monolayer height h. The larger value of h gives larger value of γ. This means the thicker membrane will require larger portion of lipids to flip to release the membrane compression and stretching. The larger value of R gives smaller value of γ. This means the larger vesicle requires smaller portion of lipids to flip to release the membrane compression and stretching. For the flat membrane, $R \to +\infty$, the value of γ converges to 0.

Combining Eq (8) and Eq (4), the difference between the two monolayers' equilibrium areas is $\Delta A_0 = A_{0,2} - A_{0,1} = 16\pi R^3 h/(R^2 + h^2)$. For the large radius $R \gg h$, we have $\Delta A_0 = 16\pi R h$, which is the same as the prediction of ADE model [24]. In this limit ΔA_0 does not in fact converge to 0 as the vesicle radius R increases, but $\Delta A_0/A_0$ does converge to 0 as R increases. According to the definition of membrane tension $\lambda = \mu_A\,(A - A_0)/A_0$ [38], we can calculate the membrane tension of each monolayer:

$$\lambda_1 = \lambda_2 = \mu_A \frac{h^2}{R^2} \tag{9}$$

From this expression, the inner and outer monolayer have the same positive tension, which means they are equally stretched after the lipid flip. For the more general situation, we need to solve Eq (7) numerically for γ, which results in distinct expressions for monolayer equilibrium area (Eq. 4). Generally, the two monolayers do not have equivalent tension.

2.2 Cylindrical membrane

For a cylindrical membrane with the length L, the radius R is defined by the radius of the mid-surface whose area is $A_m = 2\pi RL$. The area of the inner monolayer is $A_1 = 2\pi(R-h)L$ and the area of the outer monolayer is $A_2 = 2\pi(R+h)L$. The mean curvature of the inner monolayer is $c_1 = 1/2(R-h)$ and of the outer monolayer is $c_2 = 1/2(R+h)$. For the cylinder, Eq. 6 then produces the expression for γ:

$$\frac{(R-h)^2}{R^2(1-\gamma)^2} - \frac{(R+h)^2}{R^2(1+\gamma)^2} = \frac{\kappa}{\mu_A}\left[\left(\frac{1}{R-h} - c_0\right)^2 - \left(\frac{1}{R+h} + c_0\right)^2\right] \tag{10}$$

Eq (10) shows that γ is not dependent on the cylinder length L, but on the cylinder radius R, the membrane height h, lipid spontaneous curvature c_0, bending modulus κ and area elasticity modulus μ_A. By numerically solving Eq(10), we can get the value of γ for the cylindrical membrane. If the right-hand side of Eq (10) equals to 0, which may come from two situations: (i) The monolayer has $c_0 = h/(R^2 - h^2)$; (ii) The cylinder diameter is large. Then we have

$$\gamma = \frac{h}{R} \tag{11}$$

Now, γ is only dependent on the cylinder radius R and the monolayer height h. Similar to the spherical membrane, the value of γ decreases as the membrane height decreases or as the membrane radius increases, which means the thinner membrane or large membrane radius requires smaller portion of inner-layer lipids to flip to release the membrane compression and stretching. For the flat membrane $R \to +\infty$, the value of γ also converges to 0.

2.3 Planar membrane

For a flat membrane under no external forces, the two monolayers have the same area as the mid-surface $A_1 = A_2 = A_m$. Therefore no driving force exists to re-equilibrate any membrane area, giving $\gamma = 0$, $A_{0,1} = A_1$ and $A_{0,2} = A_2$.

3. Background on membrane energy for a continuum model with lipid tilt

Here, we reproduce the key principles and assumptions defining the energy that couples two leaflets via lipid tilt and curvature, as they are necessary for our subsequent derivation. A detailed description of the tilt-curvature model and relevant mathematic proofs can be found in refs [30-32]. Each monolayer of the membrane can be regarded as a solid material, whose free energy per unit volume ($\bar{\bar{E}}$) is [29]

$$\bar{\bar{E}} = \sigma_{ij}u_{ij} + \frac{1}{2}\lambda_{ijkl}u_{ij}u_{kl}, \tag{12}$$

where σ_{ij} is the stress tensor, λ_{ijkl} is the elastic modulus tensor, and u_{ij} is the strain tensor, and a summation is performed for repeated indices. For small deformations, the strain tensor is defined by $u_{ij} = \frac{1}{2}\left(\frac{\partial u_i}{\partial \xi_j} + \frac{\partial u_j}{\partial \xi_i}\right)$, where u_i is the displacement, and ξ_i represents the coordinate *x*, *y*, and *z*. After deformation, the element length *dx, dy, dz* along the three principal axes become $dx' = (1 + u_{xx})dx$, $dy' = (1 + u_{yy})dy$, $dz' = (1 + u_{zz})dz$. Considering the membrane rotational symmetry and fluidity, Eq (12) becomes [30]

$$\bar{\bar{E}} = \sigma_1(u_{xx} + u_{yy}) + \sigma_{zz}u_{zz} + \frac{1}{2}\lambda_1(u_{xx} + u_{yy})^2 + \frac{1}{2}\lambda_2 u_{zz}^2 + \lambda_3 u_{zz}(u_{xx} + u_{yy}) + 4\lambda_4(u_{xz}^2 + u_{yz}^2) \tag{13}$$

With the definition of the relative expansion of the local area as $\varepsilon = (dx'dy' - dxdy)/dxdy$, and the relative elongation of the local height as $\rho = (dz' - dz)/dz$, then we have [30]

$$u_{xx} + u_{yy} = \varepsilon, \tag{14}$$

$$u_{zz} = \rho. \tag{15}$$

The last term of Eq (13) reflects the lipid tilt: $4(u_{xz}^2 + u_{yz}^2) = T^2$ [30], where the absolute value of the lipid tilt equals to the tangent of the angle between the lipid orientation and the membrane normal, $T = \tan\theta$, see Fig 2A. In the pure tilt situation, where lipids are inclined as straight lines and their head-to-tail lengths are stretched, both the membrane area and height are unchanged [30], as shown in Fig 2A. The pure tilt model suggests that the lipid tilt is a physical term that is decoupled from the membrane area elasticity, and thus both contribute to the total membrane energy.

4. Transforming the lipid tilt energy of the Helfrich Hamiltonian to a height deformation energy

Here, with the helix insertion on one monolayer, lipids must be inclined nonlinearly to wrap around the helix. We consider the situation where both the membrane area and the lipid head-to-tail length are unchanged on this monolayer, consequently the monolayer height must be decreased because of the inclination.

Deformations of tilt and area are assumed to be small, and thus the lipid tilt can be related to the relative height change, $T^2 = (dz/dz')^2 - 1 = \frac{1}{(1+\rho)^2} - 1$. If we Taylor expand and keep terms to order ρ^2 (which will be accurate in a limit of small relative deformations $\rho \ll 1$), then $T^2 \approx 3\rho^2 - 2\rho$ and we have

4

$$\left(u_{xz}^2 + u_{yz}^2\right) \approx 3\rho^2 - 2\rho \tag{16}$$

With Eqs (14)-(16), we can rewrite Eq (13) as

$$\bar{\bar{E}} = \sigma_1\varepsilon + \frac{1}{2}\lambda_1\varepsilon^2 + \lambda_3\rho\varepsilon + (\sigma_{zz} - 2\lambda_4)\rho + \left(3\lambda_4 + \frac{1}{2}\lambda_2\right)\rho^2 \tag{17}$$

Asserting the membrane is locally incompressible implies $(1+\varepsilon)(1+\rho) = 1$. Again To second order:

$$\rho \approx -\varepsilon + \varepsilon^2 \tag{18}$$

From previous work, the relative area expansion is related to the membrane curvature [30, 31],

$$\varepsilon = zH - \frac{1}{2}z^2H^2 + z^2H_G \tag{19}$$

where H and H_G are the effective total and Gaussian curvature, respectively. When measured at the neutral surface, curvature and area deformations are decoupled energetically. Substituting Eq (19) and (18) into Eq (17) and explicitly keeping terms to second order in z , and ρ (consistent with an elastic model [30]), we have

$$\bar{\bar{E}} = \sigma_0 zH + \frac{1}{2}(\lambda_L - \sigma_0)z^2H^2 + \sigma_0 z^2 H_G + \frac{1}{2}(6\lambda_4 + \lambda_2)\rho^2 \tag{20}$$

and

$$\sigma_0 = \sigma_1 - \sigma_{zz} + 2\lambda_4 \tag{21a}$$

$$\lambda_L = 2(2\lambda_1 - 2\lambda_3 + \sigma_{zz} - 2\lambda_4) \tag{21b}$$

Taking the z-integral of Eq 20, we recover the monolayer energy per unit surface area ($\bar{E}$), ,

$$\bar{E} = \frac{1}{2}\kappa(H - H_0)^2 + \frac{1}{2}\kappa H_0^2 + \kappa_G H_G + \frac{1}{2}\int (6\lambda_4 + \lambda_2)\,\rho^2\,dz \tag{22}$$

where

$$\kappa = \int (\lambda_L - \sigma_0) z^2\,dz, \tag{23a}$$

$$H_0 = -\frac{1}{\kappa}\int \sigma_0\,z\,dz, \tag{23b}$$

$$\kappa_G = \int \sigma_0\,z^2 dz. \tag{23c}$$

Eq (22) is similar to previous works [30], except that the last term of Eq (22) arises from the monolayer height instead of the lipid tilt. Eq (22) shows we can express the monolayer height deformation as a term separated from the monolayer curvature. In the simple situation where the local monolayer height changes uniformly along *z* axis, then ρ equals to the global height change $\rho = (h - h_0)/h_0$, where h is the monolayer height and h_0 is the equilibrium value of the monolayer height without perturbation. Then the energy per area due to the monolayer height deformation is $\frac{1}{2}\kappa_h\left(\frac{h-h_0}{h_0}\right)^2$ and the height modulus, $\kappa_h = \int (6\lambda_4 + \lambda_2)\,dz$, describes the monolayer elasticity along the direction perpendicular to the monolayer surface. The total energy of the monolayer height deformation is obtained by the integral along the whole surface,

$$E_h = \int \frac{1}{2}\kappa_h\left(\frac{h-h_0}{h_0}\right)^2 dA\,. \tag{24}$$

It is noted that the tilt modulus is $\kappa_t = \int 2\lambda_4\,dz$ [30]. Then, we have $\kappa_h = 3\kappa_t + \lambda_2 h_0$. Given that λ_2 is the elastic modulus along z axis, which always has a positive value, we know the height modulus of the monolayer is larger than three times of the tilt modulus, $\kappa_h > 3\kappa_t$.

It is noteworthy that the above z-integral is performed on the neutral surface whose area is supposed to be fixed during the deformation, so the monolayer area elasticity is not included. We conclude that one can derive the monolayer height elasticity from the tilt model, and the height elasticity is decoupled from the monolayer curvature and area elasticity. It is also noted that the above derivation is performed for one membrane monolayer. For the bilayer membrane, we can calculate the height deformation energy for each monolayer and sum them up to obtain the whole height energy of the bilayer.

5. Derivation of a modified membrane energy due to helix insertion

In the previous section, we discussed the determination of membrane bending energy, area elasticity energy, and height elasticity energy. When an α-helix inserts into the outer monolayer surface of the membrane, it introduces perturbations to the membrane structure and subsequently affects the membrane energy. To account for the influence of helix insertion, we modify the membrane energy at three key points.

(i) The helix insertion reaches to the hydrophobic regions of the outer monolayer, so the neutral surface area of the outer monolayer needs to include the area occupied by the helix. In our model, the effective equilibrium area of the outer monolayer is denoted as $A_{0,2} + a$, where a is the helix insertion area. For the N-terminal α-helix of ENTH protein, a is about 2 nm^2 with 1 nm in width and 2 nm in length. It is important to note that $A_{0,2}$ remains unchanged since the helix insertion is not assumed to induce lipid flip-flop.

(ii) When the helix inserts into the outer monolayer, it causes the adjacent lipids to deform and wrap around the helix. As a result, the membrane appears thinner at the insertion site (as depicted in Fig 2B). Let's consider a helix with a radius of r inserted into a monolayer with the monolayer height of h_0. Here, we consider the situation where the helix is only shallowly inserted into the membrane, rather than immersed completely in the middle of the monolayer. We assume that the adjacent lipids tightly wrap around the helix to prevent exposure of lipid tails to the surrounding solution. The decrease in membrane height is denoted as Δh_0, whose value is the one before the membrane relaxes after the helix insertion. For one helix with r = 0.5 nm and half immersed (as shown in Fig 2B), we calculate Δh_0 to be approximately 0.29 nm, while for completely immersed, Δh_0 is around 0.57 nm. As we can see, as the helix insertion becomes deeper, the membrane height decreases at the insertion point until the helix is fully inserted. In our model, we designate a specific zone on the outer monolayer surface as the helix insertion zone, and the equilibrium height of the outer monolayer at that zone is set as $h_0 - \Delta h_0$. It is noteworthy that Δh_0 is the decrease of the monolayer equilibrium height, not the observed decrease of the monolayer height.

(iii) The spontaneous curvature of the helix insertion, denoted as $c_{0,ins}$, differs from the spontaneous curvature of the lipid monolayer c_0. In our model, when calculating the bending energy of the outer monolayer, we utilize $c_{0,ins}$ at the insertion zone, while at other zones we use c_0. Moreover, the helix insertion on the outer monolayer is assumed not to affect the spontaneous curvature of the inner monolayer.

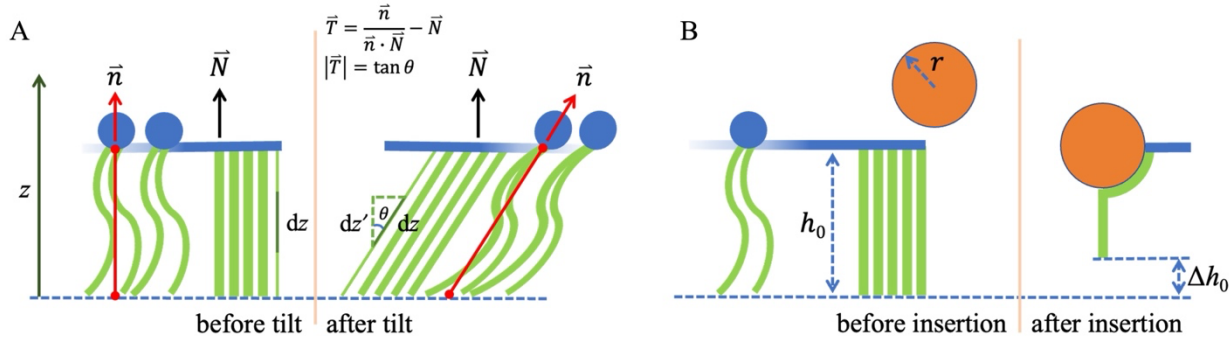

Figure 2. Schematics of lipid tilt and monolayer thinning at the insertion. (A) Definitions of monolayer normal $\vec{N}$, lipid orientation or director $\vec{n}$, and the lipid tilt $\vec{T}$. The pure tilt is drawn, where lipids are inclined constantly and their head-to-tail lengths are stretched, in order to keep the monolayer area and height unchanged (B) Schematic to show the monolayer height decreases after the α-helix insertion.

6. Relation of helix binding affinity and the membrane energy

As our previous work, we hypothesize the dissociation constant of helix binding to the membrane is [7],

$$K_D = [1M] \cdot exp\left(\frac{-\mu+\varepsilon+\Delta E}{k_B T}\right), \qquad (25)$$

where [1M] is the standard state concentration, $-\mu$ is the chemical potential due to electrostatic interactions between protein and lipids, ε is the cost of protein conformational change like the helix folding, and ΔE is the mechanical energy change of the membrane due to the helix insertion into the outer monolayer. As $-\mu$ and ε are supposed to be constant, the affinity of helix to the membrane is only dependent on the membrane energy change, $K_D \propto \exp(\Delta E/k_B T)$, and thus, a smaller value of ΔE represents a higher affinity of helix to the membrane.

Our experiments can observe wide-type ENTH proteins recruited to small unilamellar vesicles (SUVs) of different radii. By recording the protein density on the vesicle ρ_{EL}, and the PIP2 density ρ_L and the solution concentration of the protein ρ_E, we can calculate the dissociation constant of ENTH for different vesicles, $K_D = \rho_{EL}/(\rho_E \rho_L)$, as shown in Fig SX. Then substituting the value K_D to Eq (22), we get the membrane energy change due to per helix insertion, ΔE, and we further calculate $\Delta\Delta E = \Delta E - \Delta E_{ref}$, where ΔE_{ref} is chosen as the membrane energy change of the smallest vesicle (radius about 10 nm) in our experiment. The relation of $\Delta\Delta E$ and the vesicle radius R is similar to the one of K_D and R, Fig 9A and B. It shows $\Delta\Delta E$ increases monotonically with the vesicle radius R.

Methods

I. Continuum membrane model

1. Finite element method

In this work, we use three layers of triangular mesh to represent the bilayer membrane, with the top and bottom layers of the mesh mimicking the neutral surface of each monolayer and the middle layer of the mesh mimicking the mid-surface of the bilayer membrane. The neutral surface is an intra-monolayer plane on which the deformations of monolayer bending and area elasticity are energetically decoupled [35]. Approximately, the neutral surface is located at the interface dividing the lipid polar heads and the hydrocarbon tails. The zone between the mesh layers represents the lipid hydrocarbon tails. Therefore, the bilayer height here refers to the hydrocarbon height of the bilayer membrane [39].

To build the three layers of triangular mesh, we first build the one as the outer monolayer mesh, and then move each vertex by h_0, the monolayer height value, to get the mid-surface mesh, and move each vertex by $2h_0$ to get the inner monolayer mesh. The movement direction depends on the geometry of the membrane. For example, for the spherical membrane, the movement is towards the center of the sphere. We call these three mesh-layers as triplets, because they have the same number of vertices and triangle elements, and the vertex indexes have the one-to-one correspondence between the three mesh-layers, so as the indexes of triangle elements. We calculate the area and curvature formed on each triangle on the top and bottom mesh-layers. We also calculate the distance between two elements on top and middle mesh-layer respectively with the same element index and project it to the normal of the outer element, then we get the local height of the outer monolayer. Likewise, we can calculate the local height of the inner monolayer.

To simulate that one helix insertion is bound on the outer monolayer surface, we select several adjacent triangles on the outer mesh to represent the location of the insertion, and the area sum of these selected triangles is the insertion size a. The spontaneous curvature of the selected triangles is set as $c_{0,ins}$, the spontaneous curvature of the helix insertion which is different from lipid monolayer spontaneous curvature c_0. The monolayer height has an equilibrium value h_0, except the selected triangles that is set as $h_0 - \Delta h_0$. The equilibrium area of outer monolayer is set as $A_{0,2} + a$, and the equilibrium area of inner monolayer is set as $A_{0,1}$.

The total energy of the membrane is calculated by the Eq (1) combined with its terms Eq (2), Eq (3) and Eq (24). It is noteworthy that in Eq (2) the curvature energy is defined by the integration on the equilibrium area of each monolayer [23]. Generally, the curvature energy is calculated on

the actual surface. In the finite-element analysis, the curvature energy for each monolayer is defined as [7, 18],

$$E = \int \frac{1}{2}\kappa[2H(\boldsymbol{s}) - c_0(\boldsymbol{s})]^2\sqrt{a}ds^1ds^2, \qquad (25)$$

where $\{s^1, s^2\}$ is the curvilinear coordinates on the curved surface, and $\boldsymbol{s} = \boldsymbol{s}(s^1, s^2)$ represents each point on the surface in three-dimensional space.

The force on each vertex is calculated by means of the finite element analysis, see Supporting Information. We perform computational simulations to minimize the energy of the membrane and get the structure and energy of the bilayer membrane at the equilibrium state. For all parameters and their values, please see Table 1. The parameter value of DOPC membrane will be chosen as the default in our simulation unless extra notice is given.

Table 1. Parameters of the continuum membrane model and values for 4 types of lipid membranes.

Parameter	Symbol (unit)	DOPC	DLPC	POPC	DPPC
Bilayer hydrocarbon height	$2h_0$ (nm)	2.71 [39]	2.09 [40]	2.75 [41]	2.85 [39]
Monolayer spontaneous curvature	c_0 (nm^{-1})	−0.04 [42]	+0.11 [42]	+0.01 [42]	+0.05 [42]
Bilayer bending modulus	2κ (k_BT)	19.4 [21]	20.4 [21]	25.7 [21]	27.5 [21]
Tilt modulus	κ_t (pN/nm)	89 [21]	55 [21]	73 [21]	43 [21]
Bilayer area modulus	$2\mu_A$ (pN/nm)	265 [43]	234 [44]	255 [44]	231 [44]
Monolayer height modulus	κ_h (pN/nm) *	354	289	328	274
Insertion spontaneous curvature	$c_{0,ins}$ (nm^{-1})	0.3 [7]	0.3 [7]	0.3 [7]	0.3 [7]
Decrease of the equilibrium height	Δh_0 (nm) MD	0.3	0.3	0.25	0.4

Note: * The height modulus is approximated by $\kappa_h = \kappa_t + 2\mu_A$ which satisfies our theory prediction $\kappa_h > 3\kappa_t$. MD The equilibrium height decrease Δh_0 is validated by our molecular dynamic simulations.

2. Locally finer mesh around the insertion

The helix insertion on the membrane will generate the membrane deformation locally distributed around the insertion. To describe the local deformation more precisely in the finite element method, we should use finer mesh. However, to make the mesh finer everywhere will make the simulation expensive. Instead, we choose to build the finer mesh only around the insertion zone locally, while zones further from the insertion keeps non-finer, FigS1 A and B. This locally finer mesh includes regular patches and three types of irregular patches. The regular patch is the triangle who has 12 one-ring vertices, or all its three vertices have the valence of 6, while the irregular patch is the one whose one-ring vertices are not 12, or at least one of its vertices doesn't have the valence of 6, see the supporting Table S1. For the irregular patch, subdivision will be conducted to make it into 4

smaller patches, among which 2 or 3 are regular patch and the extra irregular one needs further subdivision.

The area of the finer mesh is not a key parameter to influence the energy calculation as long as the area covers the local perturbation of the membrane induced by the helix, FigS1 C. Our results show the perturbation of the membrane generated by one helix always spreads within a limited area, smaller than 2 nm in radius, which will be shown later in the Results section. Therefore, by default, the local area of the finer mesh is set with the radius 5 nm.

We notice that the membrane energy decreases as the mesh becomes finer around the insertion, FigS1 D. Though making the mesh infinitely finer around the insertion improves the mathematical precision of the calculation, yet we think the physical meaning is weakened. The lipid on membrane has an area about 0.5 nm^2 in average, which suggests the length of 0.7 nm for the triangle edge on the mesh. The finer mesh with the triangle edge far smaller than 0.7 nm should not represent the physical properties of the membrane. Therefore, we set the smallest triangle edge as 0.5 nm when we build the locally finer mesh.

3. Boundary conditions

Our continuum membrane model can simulate different membranes of variable shapes, such as vesicle, tubule and flat membranes. The vesicle membrane has an enclosed structure that doesn't have a boundary. However, the tubule and flat membranes have edges that need boundary conditions to constraint the movement. We have three types of boundary conditions: free, fixed and periodic boundaries, which have been successfully developed and employed in our previous one-layered continuum membrane model [7]. For the free boundary, positions of vertices at the edge are dependent on its neighbor vertices' positions regardless of the nodal forces on the edge vertices, FigS 2A. For the fixed boundary, the edge vertices are fixed and can't move during the simulation, FigS 2B. For the periodic boundary, we create three layers of temporary vertices outside the edge of the mesh, called ghost vertices, to help calculate the position updates of the edge vertices. The locations of ghost vertices are determined by translation of the mesh vertices at the opposite edge, FigS 2C. We perform the boundary condition on each of the two monolayers separately, but we don't allow the two monolayers have different types of boundary conditions. In this paper, the periodic boundary is the default for flat or tubular membranes, unless the extra

notice is given. The code is available open source at https://github.com/Yibenfu/triple-layer-continuum-membrane-model.

III. Experiments

1. Materials

DOPC (1,2-dioleoyl-*sn*-glycero-3-phosphocholine), POPC (1-palmitoyl-2-oleoyl-glycero-3-phosphocholine), DLPC (1,2-dilauroyl-sn-glycero-3-phosphocholine), DPPC (1,2-dipalmitoyl-sn-glycero-3-phosphocholine), and DOPI(4,5)P2 (1,2-dioleoyl-sn-glycero-3-phospho-[1'-myo-inositol-4',5'-bisphosphate] [ammonium salt]) were purchased from Avanti Polar Lipids. DPPI(4,5)P2 (Phosphatidylinositol 4,5-bisphosphate diC16) was purchased from Echelon Biosciences. DP-EG10-biotin (dipalmitoyl-decaethylene-glycol-biotin) was generously provided by Darryl Sasaki from Sandia National Laboratories, Livermore, CA. Texas Red-DHPE (Texas Red 1,2-dihexadecanoyl-*sn*-glycero-3-phosphoethanolamine triethylammonium salt), NeutrAvidin, and Zeba spin desalting columns (7K MWCO, 5 mL) were purchased from Thermo Fisher Scientific. TCEP (tris(2-carboxyethyl) phosphine hydrochloride), PMSF (phenylmethanesulfonyl fluoride), EDTA-free protease inhibitor tablets, imidazole, PLL (poly-L-lysine), and ATTO-488 NHS-ester were purchased from Sigma-Aldrich. Sodium chloride, HEPES (4-2(2-hydroxymethyl)-1-piparazineethanesulfonic acid), IPTG (isopropyl-β-D-thiogalactopyranoside) and β-mercaptoethanol were purchased from Fisher Scientific. Amine reactive PEG (mPEG-succinimidyl valerate MW 5000) and PEG-biotin (biotin-PEG SVA MW 5000) were purchased from Laysan Bio, Inc. Glutathione Sepharose 4B was purchased from GE Healthcare. All reagents were used without additional purification.

2. Protein Purification and Labeling

ENTH was purified and labeled as previously described [1]. Briefly, ENTH was expressed as a fusion protein containing N-terminal glutathione-S-transferase (GST) in *E coli* BL21. These cells were lysed and centrifuged, and the protein was purified from the supernatant with affinity columns in a three-step process. First, the supernatant was incubated with glutathione agarose beads, and excess cell material was washed from the bound proteins. Thrombin was used to cleave the proteins from the beads, and excess thrombin was removed with *p*-aminobenzamidine-agarose. The purity of the protein was verified using SDS-PAGE and UV-Vis spectroscopy. The product

was then concentrated and stored at -80C after snap freezing in liquid nitrogen. The purified protein was labeled with ATTO488 NHS-ester that was pre-dissolved in DMSO. The total DMSO in the protein/dye mixture was kept to less than 1.5% by volume. The mixture was incubated at room temperature for 30 minutes at a 2x stoichiometric excess of ATTO488 NHS-ester. Excess dye and DMSO were removed by running the reaction solution through a 7k Zeba Spin column.

3. SUV Prep

Lipid aliquots were brought to room temperature and combined appropriately to achieve the following mixtures:

- 87.5% DOPC, 10% DOPI(4,5)P2, 2% DP-EG10-biotin, 0.5% Texas Red-DHPE
- 87.5% POPC, 10% DOPI(4,5)P2, 2% DP-EG10-biotin, 0.5% Texas Red-DHPE
- 87.5% DLPC, 10% DOPI(4,5)P2, 2% DP-EG10-biotin, 0.5% Texas Red-DHPE
- 87.5% DPPC, 10% DPPI(4,5)P2, 2% DP-EG10-biotin, 0.5% Texas Red-DHPE

All solvents for combined lipids were adjusted accordingly to yield a solution that was 65:35:4 Chloroform:Methanol:Water by volume. These solutions were evaporated under a nitrogen stream to create a lipid film and dried overnight under vacuum. The lipid film was rehydrated to a final lipid concentration of 100 uM in 25 mM HEPES (pH 7.4), 150 mM NaCl, 0.5 mM EDTA, and 0.5 mM EGTA. This lipid suspension was cycled three times through a freeze/thaw cycle (2 minutes to freeze in liquid nitrogen, and 2 minutes to thaw in a 60° C water bath). It was followed by extrusion through a 50nm and 200nm polycarbonate filter with average diameters of 79 nm and 127 nm, respectively, determined by dynamic light scattering. The two populations of SUVs were then mixed together to generate a broad range of vesicle diameters.

4. Tethering and imaging

SUV's were tethered as previously described [5]. Briefly, glass cover slips were cleaned and then passivated with a layer of biotinylated PLL-PEG. Vesicles with 2 mol% DP-EG10-Biotin were tethered to this surface using NeutrAvidin. Excess vesicles and NeutrAvidin were rinsed away. Labeled ENTH was then incubated with the tethered vesicles at the desired concentrations and imaged after a minimum of 10 minutes. Proteins and vesicles were visualized on a laser scanning confocal microscope (Leica Stellaris 5) using 488 and 561 nm lasers for excitation for the proteins and lipids, respectively.

Results

I. Membrane deformations induced by the helix insertion in the continuum model with comparison to MD simulations

1.Membrane thins around the helix insertion

The helix insertion can induce local membrane deformations. By simulating the helix insertion on the top monolayer of the flat membrane, our continuum membrane model shows the top monolayer thins around the insertion zone, Fig 3A and B. The height deformation of the top monolayer has a radial distribution around the insertion, Fig 3A, showing a monotonical decrease of the height when closer to the helix insertion, Fig 3B. Because the two monolayers closely contact, the mechanical deformation on the top monolayer can affect the bottom monolayer, which results in the perturbation of the bottom monolayer height. Like the top monolayer, the height deformation of the bottom monolayer also has a radial distribution. However, unlike the top monolayer, the bottom monolayer doesn't show a monotonical decrease of its height. It also shows that the height deformation of the two monolayers will be more parent if the value of Δh_0 is larger, Fig 3B. According to our model, the larger Δh_0 corresponds to the deeper insertion of the helix into the monolayer. Therefore, Fig 3B means the deeper insertion of the helix can induce larger perturbation of the two monolayers. Our simulations also show that the height perturbation because of the helix insertion is always limited in a small area with the perturbation decaying drastically where it is about 2.5 nm farther from the insertion, as shown in Fig 3B.

2. Deformed membrane shape is dependent on insertion depth and membrane height.

The helix insertion also perturbs the membrane shape. The helix spontaneous curvature, $c_{0,ins} >$ 0 nm^{-1}, tends to make the top monolayer bulge up around the insertion. However, the inclines of lipids adjacent to the insertion tend to make the top monolayer dent down around the helix. These two factors work together to determine the equilibrium shape of the membrane. In our simulations here, we fix the value of the helix spontaneous curvature, $c_{0,ins}$ = 0.3 nm^{-1} as suggested by our previous study [7], and investigate how the helix insertion affects the membrane shape. The incline of lipids around the insertion is dependent on the insertion depth, which is characterized by Δh_0. Our continuum membrane model shows that the small Δh_0 gives the small bulge on the membrane up-surface, but the large Δh_0 gives the dent on the membrane up-surface, Fig 3C. This means, for

the shallow insertion, the helix spontaneous curvature will slightly dominate the membrane up-surface shape to make a small bulge, but for the deep insertion, the large incline of the lipids will dominate the membrane up-surface shape to make a dent. The middle-surface and down-surface of the membrane are also perturbed because of the helix insertion on the top monolayer, Fig 3C. The down-surface is always arched up towards the top of the membrane, with the arch being larger if the insertion is deeper. The middle-surface of the membrane is also arched up in our simulations, though its shape is not smooth as the down-surface. Besides the insertion depth, our results show the height of the membrane can regulate the membrane shape too. With the fixed insertion depth, Δh_0 = 0.3 nm, the up-surface of the membrane becomes more bulged if the membrane is thicker, meanwhile the down-surface is less arched and the middle-surface is still unsmoothly arched, Fig 3D. To comprehensively consider the membrane properties, we perform simulations with helix insertion on DLPC membrane. Compared to DOPC membrane, the DLPC membrane shows a more dented up-surface, more perturbed middle-surface and slightly more arched down-surface, Fig 3E. These results mean the deformed membrane shape induced by the helix insertion is dependent on properties of both the helix insertion and membrane.

3.Optimized parameters with comparison to MD simulations.

Our results above show the helix spontaneous curvature $c_{0,ins}$, value of Δh_0 and membrane height $2h_0$ together determine the membrane deformation after the helix inserted to one monolayer. The membrane height can be directly found from the previous experimental works, and the helix spontaneous curvature has supported values, as shown in Table 1. However, the value of Δh_0 has not been determined. To determine the optimal value of Δh_0, we compare the simulation results of our model with molecular dynamic simulations. MD simulation with the ENTH helix shows that the membrane thins around the insertion, with the up-surface dented down and middle- and down-surface arched up slightly, which is consistent with results of our continuum membrane model. The decrease of the membrane height in MD simulations is observed about 0.75 Å for DOPC membrane. To best fit the MD results, we find $\Delta h_0 \approx 0.30$ nm for the helix insertion on DOPC or DLPC membranes, as shown in Fig 3C and E, respectively. According to our analysis above, $\Delta h_0 \approx 0.30$ nm corresponds to the situation where the helix is half immersed to the membrane, Fig 2B.

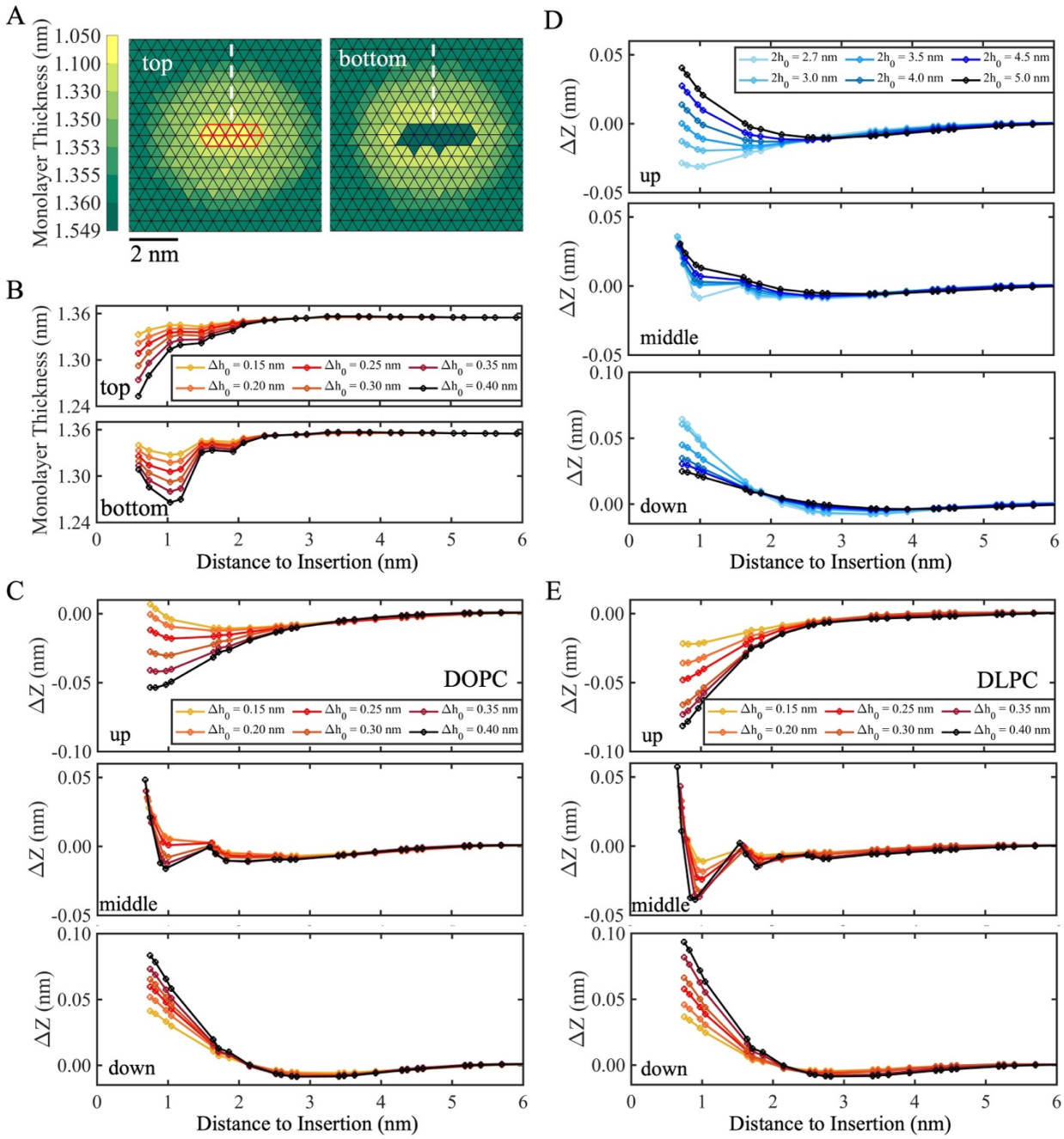

Figure 3. Membrane is deformed because of the helix insertion. (A) The height deformation of the DOPC membrane has a radial distribution around the helix insertion. (B) The height deformation of the DOPC membrane decays as the distance from the insertion is longer, dependent on Δh_0. The membrane height is calculated on triangles that are along the while dashed line as shown in (A). (C) The DOPC membrane is perturbed on its shape because of the helix insertion, dependent on Δh_0. (D) The DOPC membrane is perturbed on its shape because of the helix insertion with Δh_0 = 0.3 nm, regulated by the membrane height $2h_0$. (E) The DLPC membrane is perturbed on its shape because of the helix insertion, dependent on Δh_0. MD simulations captured the lipid trace around the ENTH α-helix with the membrane lipid DOPC and DLPC respectively. The sn-1 chain is shown in blue. The sn-2 chain is shown in green. The extend

headgroup region is red. The CHARMM C24 atom (the approximate neutral surface) is shown in purple. The height of the C24 atom is shown as the black dots. Since the bottom layer of the membrane keeps almost flat in our MD simulations, the height of the C24 atom should satisfy the same curve as the membrane height. We translationally move the black dots up or down to make their right-side overlap with the height of the continuum membrane model.

II. Material properties of the membrane and the helix impact curvature sensing

1. Two-leaflet model captures curvature sensing

To see the curvature sensing of the helix insertion, we ran simulations with one α-helix bound on vesicles of different radii. Our simulations show that the membrane energy change ΔE due to one helix insertion increases monotonously as the vesicle becomes larger, Fig 4A, which means the helix has higher affinity to the small vesicle than to the large vesicle. By analyzing the three components of the energy, i.e. the curvature energy, the area elasticity energy, and the height elasticity energy, we found they all increase as the vesicle is larger, which suggests all these three types of energy contribute positively to the curvature sensing phenomenon. We also draw $\Delta\Delta E$ *vs* vesicle radius R, Fig 4B, where $\Delta\Delta E = \Delta E - \Delta E(\mathrm{R=15nm})$ represents the difference of the membrane energy change relative to the one of the smallest vesicle $R = 15$ nm. It can be seen from Fig 4B that the curvature energy and area elasticity energy increase faster than the height elasticity energy when the vesicle become larger, which suggests that the curvature sensing of α-helix insertion is mainly dependent on the membrane bending and the area change.

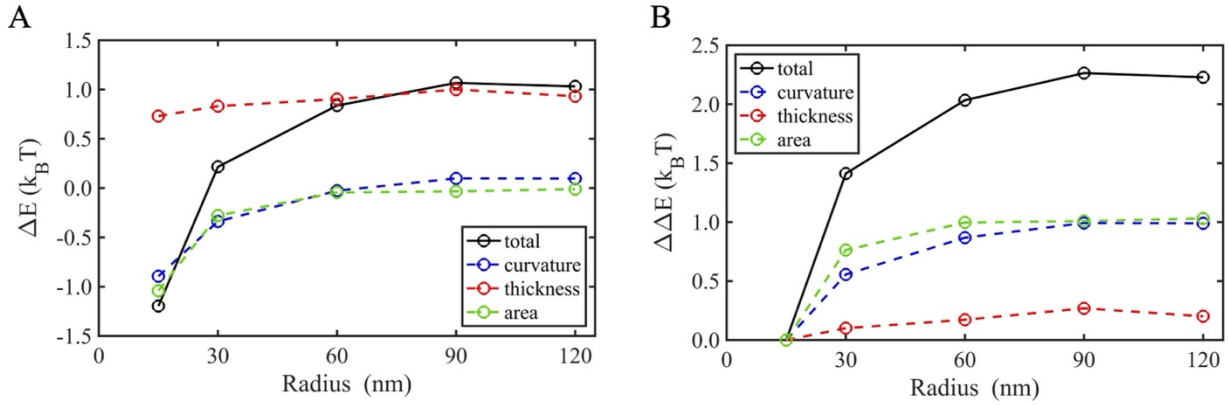

Figure 4. Curvature sensing of one α-helix. (A) Membrane energy change because of one α-helix insertion vs vesicle radius. (B) Replot of (A) with $\Delta\Delta E = \Delta E - \Delta E(\mathrm{R=15nm})$. Simulations were performed with DOPC membrane parameters with the bilayer hydrophobic height as 4.0 nm , and the helix insertion has the area of 2 nm^2 and spontaneous curvature of 0.3 nm^{-1}.

2. Thicker membrane enhances membrane binding and curvature sensing.

To investigate the effect of the membrane height on the helix insertion on the membrane, we ran simulations of vesicles with the same radius but variable height. Our results show that by increasing the membrane height, ΔE becomes smaller, Fig 5A, which means the helix insertion has a higher affinity to the thicker membrane. By the comparison of the three energy components, we can tell that the height sensing is dominated by the height elasticity energy, slightly attributed to the curvature energy, and not dependent on the area elasticity energy. Our results also show the height sensing phenomenon can happen on vesicles of any radius, Fig 5B. It is noted that the curvature sensing is robustly captured no matter how thick the membrane is, Fig 5C. By drawing $\Delta\Delta E$ *vs* vesicle radius R, Fig 5D, where $\Delta\Delta E = \Delta E - \Delta E(\mathrm{R=15nm})$ as in Fig 4B, we can clearly see that the curvature sensing of the helix insertion is more obvious on the membrane with the larger height.

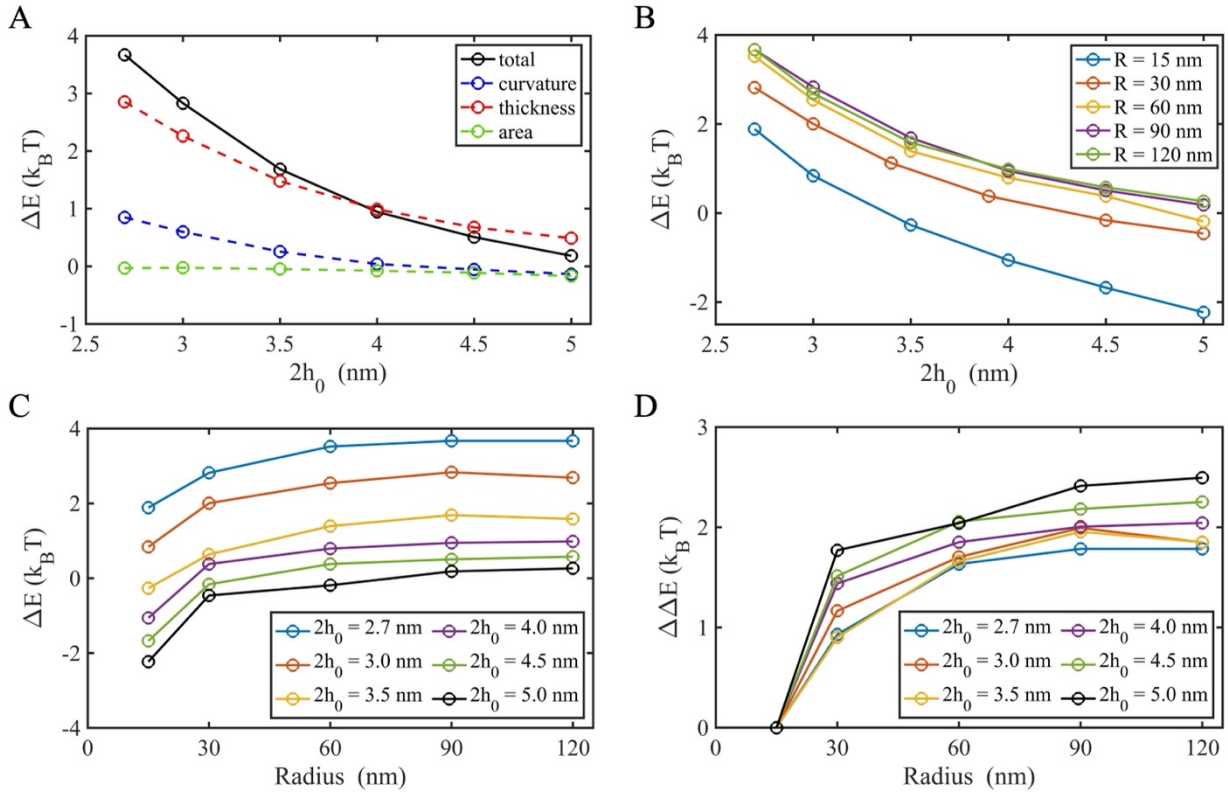

Figure 5. Membrane height affects curvature sensing. (A) Membrane energy change ΔE because of one α-helix insertion vs membrane height $2h_0$. Simulations were performed with vesicle radius $R = 90$ nm. (B) Relation of ΔE and $2h_0$ on vesicles of different radii. (C) Relation of ΔE and vesicle radius with different height $2h_0$. (D) Replot (C) with

$\Delta\Delta E = \Delta E - \Delta E(\mathrm{R=15nm})$. Simulations were performed with DOPC membrane parameters, and the helix insertion has the area of 2 nm^2 and spontaneous curvature of 0.3 nm^{-1}.

3. Larger deformation of local lipids strengthens the binding affinity and curvature sensing. The change of the membrane height Δh_0 at the insertion results from the lipid deformation adjacent to the α-helix. The more significant deformation of lipids gives a more considerable decrease in membrane height. Our simulations show Δh_0 can influence the α-helix affinity to the membrane and its curvature sensing ability. Our results show a larger value of Δh_0 makes ΔE become larger, Fig 6A. It means the α-helix will have a lower affinity to bind to the membrane if its insertion makes the lipids more deformed because it will cost more energy. Meanwhile, the curvature sensing ability of the α-helix will become stronger if its insertion makes the lipids more deformed, Fig 6B. Previous works have proposed that the α-helix has different insertion depth on the membrane [45]. Since the insertion depth can affect the value of Δh_0, we suppose ENTH proteins may regulate their affinity and curvature sensing by changing their insertion depth.

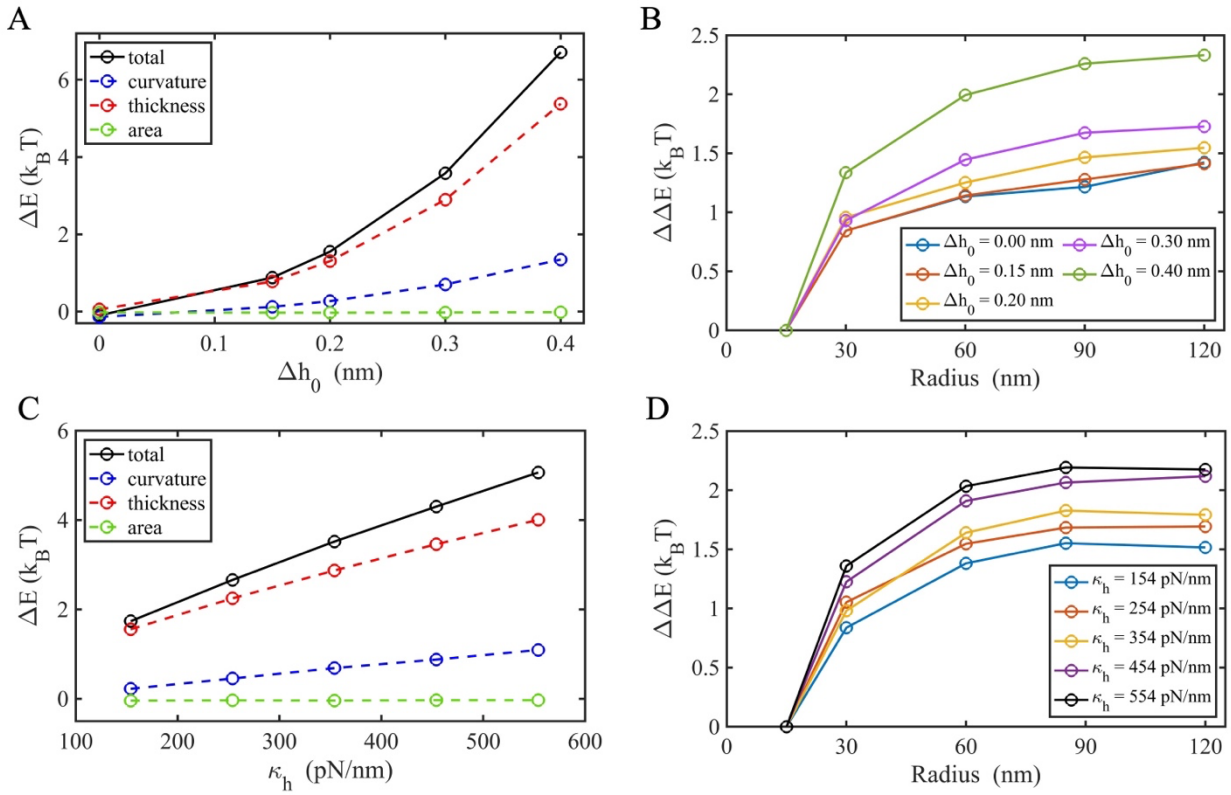

Figure 6. Lipid deformation affects curvature sensing. (A) Membrane energy change ΔE because of one α-helix insertion depends on the equilibrium value of the height decrease at the insertion Δh_0. Simulations were performed with vesicle radius R = 60 nm. (B) Relation of $\Delta\Delta E$ and vesicle R is regulated by Δh_0. Here, $\Delta\Delta E = \Delta E - \Delta E$(R=15nm).

4. The lipid spontaneous curvature modulates curvature sensing.

We ran simulations of the α-helix insertion on membranes with different lipid compositions by changing the spontaneous curvature of the two monolayers. Different lipids have different spontaneous curvaturesc_0, for example, DOPC has a negative spontaneous curvature of −0.04 nm^{-1}, and DLPC has a positive spontaneous curvature of +0.11 nm^{-1}, see the Table 1. Our simulations show that by increasing the lipid spontaneous curvature from −0.25 nm^{-1} to −0.06 nm^{-1}, the membrane energy change ΔE is increased, Fig 7A. These results suggest the α-helix insertion has a higher affinity to the membrane that has lipids with more negative spontaneous curvature. With the calculated ΔE, we can calculate the relative binding equilibrium constant $K_{eq}/K_{eq0} = \exp[-(\Delta E - \Delta E_0)/k_B T]$, where ΔE_0 is the membrane energy change because of one helix insertion on the reference vesicle with the spontaneous curvature $c_0 = -0.06$ nm^{-1}, and K_{eq0} is the corresponding equilibrium constant for the helix insertion binding on this reference vesicle. Our results show K_{eq}/K_{eq0} increases as the lipid spontaneous curvature becomes more negative, and the tendency agrees well with the previous experimental data. With these results, we suppose that ENTH α-helix should have different binding affinities to different membranes, and the curvature sensing phenomenon would also be changed synchronously.

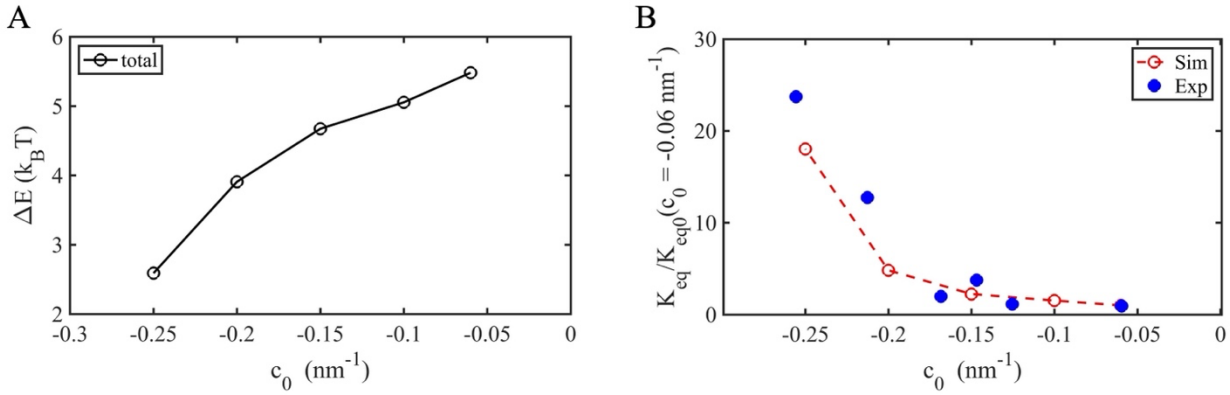

Figure 7. Helix insertion senses the lipid spontaneous curvature c_0. (A) Membrane energy change ΔE because of one α-helix insertion depends on the lipid spontaneous curvature c_0. (B) The calculated relation of K_{eq}/K_{eq0} with c_0. Here, Simulations were performed with vesicle radius R = 28 nm, and the helix insertion size is 4 nm^2 (4 nm in length and 1 nm in width), consistent with previous setup.

5. ENTH helix does not sense membrane asymmetry.

Plasma membrane is famous for the asymmetry between its two monolayers, which is maintained to play significant biological roles. We wonder whether the membrane asymmetry can affect ENTH helix insertion on the membrane. We performed simulations with one helix insertion on the outer monolayer of the vesicle with the radius 60 nm, and changed the spontaneous curvature of the inner monolayer c_0 to simulate the two monolayers are composed of different lipid compositions. Our simulations show the membrane energy change due to the helix insertion only slightly varies with the inner monolayer c_0, Fig 8A. Although the curvature energy and area energy is more influenced by the inner c_0 than the height energy, yet the total energy is only slightly fluctuated with inner c_0. We further ran more simulations with different insertion depth or Δh_0. It shows the larger Δh_0 doesn't make it more drastic for the membrane energy change with the inner c_0, and the energy fluctuation is always within 0.5 k_BT (Fig 8B), which is smaller than the thermodynamics so that no experiments can observe. Therefore, we conclude that the ENTH helix insertion on one monolayer of the membrane doesn't have a strong sense of the membrane asymmetry.

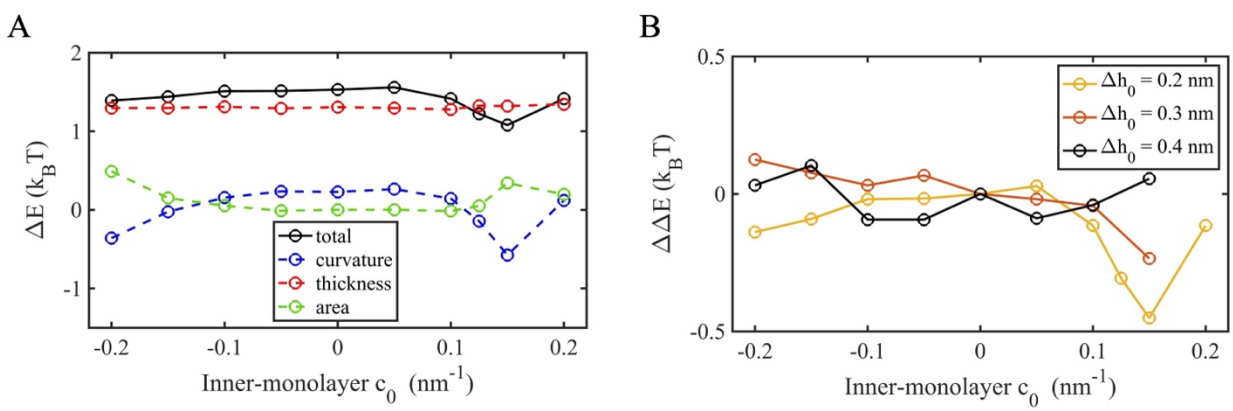

Figure 8. Helix insertion can't sense the membrane asymmetry. (A) Relation between membrane energy change ΔE because of one helix insertion and the lipid spontaneous curvature c_0 of the inner monolayer. (B) Δh_0 doesn't regulate much on the relations of (A). Here, $\Delta\Delta E = \Delta E - \Delta E(c_0 = 0\ \text{nm}^{-1})$. The simulations were performed with vesicle radius $R = 60$ nm, and the helix insertion on the outer monolayer has the size 2 nm^2 (2 nm in length and 1 nm in width). The membrane parameters follow DOPC membrane.

III. Comparison of model predictions with *in vitro* experiments.

1. **Model captures the curvature sensing ability of helix insertion on different lipid compositions.**

To test our model predictions, we performed *in vitro* experiments measuring curvature sensing of the ENTH domain to vesicles of varying radii, as in previous work[46], but here with variations to lipid composition. To eliminate changes to chemistry that could influence recruitment of ENTH to the membranes, we kept the PIP_2 concentration the same and compared DOPC, DLPC, POPC, and DPPC containing liposomes. Thus, the head group phosphatidyl choline remained unchanged but the tail groups varied. The expected moduli for these lipids are known and collected in Table 1. Because the tail groups influence all moduli, it is not obvious how the preference of ENTH to highly curved membrane will vary. From experiments, we see that ENTH shows stronger curvature sensing, or a higher relative affinity for highly curved membranes, when they are composed of DOPC compared to DLPC. The change in binding energy between the largest and smallest vesicle for DOPC reaches 1.9 k_BT, while for DLPC membrane it is closer to 1.5 k_BT. POPC is quite similar to DOPC.

We mimicked these same lipid compositions with our continuum double leaflet-model using parameters in Table 1 and the same vesicle radii as in the experiment. The simulations show excellent agreement to the experiment, predicting that curvature sensing is stronger for DOPC compared to DLPC, despite a nearly identical bending modulus for both lipids (Fig 9). A detailed analysis of our simulation data shows the curvature bending and area elasticity energies increase more drastically with vesicle radius when the ENTH helix inserts on DOPC, which is a thicker lipid with a higher tilt modulus.

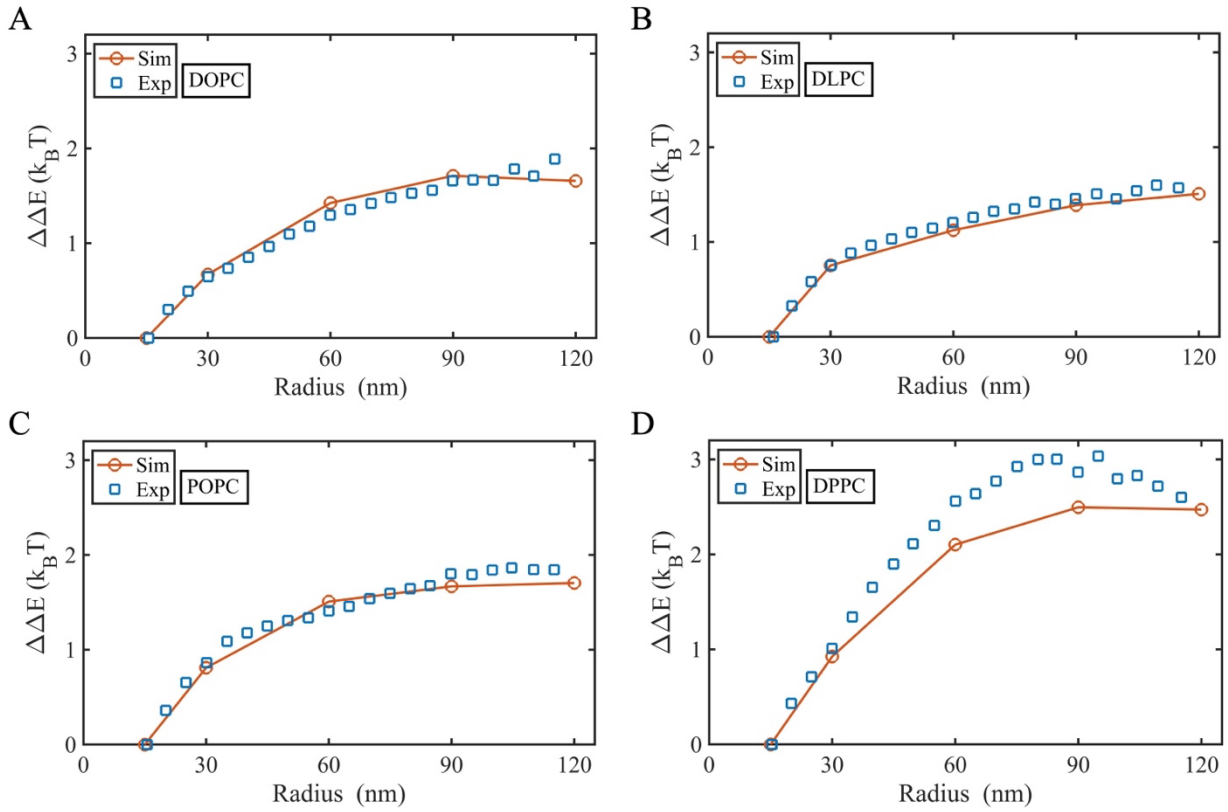

Figure 9. Comparison between in vitro experiment and computational results. (A) ENTH helix binding to membrane of DOPC lipid. (B) ENTH helix binding to membrane of DLPC lipid. (C) ENTH helix binding to membrane of POPC lipid. (D) ENTH helix binding to membrane of DPPC lipid. The parameters in the simulations are as in the Table 1.

Discussion

Our results demonstrate how continuum membrane models that capture key mechanical properties of the membrane including bending modulus, tilt modulus, area compressibility, and bilayer height can accurately capture the structural and energetic changes to the bilayer upon amphipathic helix insertion. Hence, despite lacking molecular-level details on lipid packing and reorganization around the helix insertion, they can nonetheless faithfully capture the local perturbations to the double-leaflet bilayer driven by the helix-induced changes to area, spontaneous curvature, and membrane height. We carefully assessed how variations in material parameters of an explicit double-leaflet bilayer will change the curvature sensing by proteins inserted into the outer leaflet. We showed how the height of the bilayer, which varies as lipid tail group varies, will increase the curvature sensing by protein insertions, driving a stronger binding selectivity for more highly curved membranes. Symmetric leaflets with a negative spontaneous curvature also produce

stronger curvature sensing. In contrast, asymmetry between the leaflets has negligible impact on curvature sensing, indicating the phenomenon is primarily driven by the properties of the outer leaflet. More deeply inserted helices also drive stronger curvature sensing. Our model is capable of arbitrary topologies, with explicit implementations for membranes initialized as spheres, cylinders, and flat surfaces. It can be immediately applied to quantify membrane remodeling by additional mechanisms such as protein scaffolding, and is available open source.

Our double-leaflet model improves upon the single-surface model of the bilayer by explicitly capturing bilayer height and asymmetries between leaflets that are widespread in biological membranes. One limitation of the model is that we excluded Gaussian curvature terms because we kept the topology of our membrane surfaces unchanged. However, some protein driven perturbations like transmembrane proteins and pore formation can affect topology so this term would need to be added. Another limitation of any continuum model is that it is difficult or impossible to account for inhomogenity in the lipid distributions across the surface, which could affect local mechanical properties. A partitioning of lipids by type could influence flip-flop across the membrane, for example.

An interesting outcome of our model is that we can quantify the extent of membrane that is locally perturbed by the single helix insertion. Both our continuum membrane model and MD simulations show that the helix of ENTH protein only perturbs a small area on the membrane of no more than 1.5nm from the center of the helix. Given that the ENTH protein is ~4nm in length and ~1.2nm in width, the perturbation area of two ENTH helix insertions has minimal overlap even when they are adjacent. This indicates that two helices will be effectively independent of one another, each contributing the same energetic change when inserted to the membrane with negligible cooperativity. However, as the length of the helix increases, the perturbed area of the membrane extends out further, which could lead to coupling between adjacent helices. In previous work that studied infinitely long helix insertions on 3D flat membranes using classical elasticity theory, the helices did impact one another energetically [30, 31]. We thus predict that the length of the helix has a further role for inducing cooperativity between multiple helix insertions on flat or curved membranes. Overall, this model provides an experimentally validated tool that will provide a powerful resource for characterizing how properties of biological membranes and the proteins that interact with them drive functional membrane remodeling.

References

1. Taylor, M.J., D. Perrais, and C.J. Merrifield, *A High Precision Survey of the Molecular Dynamics of Mammalian Clathrin-Mediated Endocytosis.* Plos Biology, 2011. **9**(3).
2. Collins, A., et al., *Structural Organization of the Actin Cytoskeleton at Sites of Clathrin-Mediated Endocytosis.* Current Biology, 2011. **21**(14): p. 1167-1175.
3. Woods, B.L. and A.S. Gladfelter, *The state of the septin cytoskeleton from assembly to function.* Curr Opin Cell Biol, 2021. **68**: p. 105-112.
4. Baumgart, T., et al., *Thermodynamics and mechanics of membrane curvature generation and sensing by proteins and lipids.* Annu Rev Phys Chem, 2011. **62**: p. 483-506.
5. Zeno, W.F., et al., *Synergy between intrinsically disordered domains and structured proteins amplifies membrane curvature sensing.* Nature Communications, 2018. **9**(1): p. 4152.
6. Capraro, B.R., et al., *Curvature sensing by the epsin N-terminal homology domain measured on cylindrical lipid membrane tethers.* J Am Chem Soc, 2010. **132**(4): p. 1200-1.
7. Fu, Y.B., et al., *A continuum membrane model can predict curvature sensing by helix insertion.* Soft Matter, 2021. **17**(47): p. 10649-10663.
8. Sodt, A.J. and R.W. Pastor, *Molecular Modeling of Lipid Membrane Curvature Induction by a Peptide: More than Simply Shape.* Biophysical Journal, 2014. **106**(9): p. 1958-1969.
9. Gonzalez-Rubio, P., et al., *Amphipathic-Lipid-Packing-Sensor interactions with lipids assessed by atomistic molecular dynamics.* Biochimica Et Biophysica Acta-Biomembranes, 2011. **1808**(9): p. 2119-2127.
10. Vanni, S., et al., *Amphipathic Lipid Packing Sensor Motifs: Probing Bilayer Defects with Hydrophobic Residues.* Biophysical Journal, 2013. **104**(3): p. 575-584.
11. Gomez-Llobregat, J., F. Elias-Wolff, and M. Linden, *Anisotropic Membrane Curvature Sensing by Amphipathic Peptides.* Biophysical Journal, 2016. **110**(1): p. 197-204.
12. Cui, H.S., E. Lyman, and G.A. Voth, *Mechanism of Membrane Curvature Sensing by Amphipathic Helix Containing Proteins.* Biophysical Journal, 2011. **100**(5): p. 1271-1279.
13. Campelo, F., H.T. McMahon, and M.M. Kozlov, *The hydrophobic insertion mechanism of membrane curvature generation by proteins.* Biophysical Journal, 2008. **95**(5): p. 2325-2339.
14. Campelo, F. and M.M. Kozlov, *Sensing Membrane Stresses by Protein Insertions.* Plos Computational Biology, 2014. **10**(4).
15. Helfrich, W., *Elastic Properties of Lipid Bilayers - Theory and Possible Experiments.* Zeitschrift Fur Naturforschung C-a Journal of Biosciences, 1973. **C 28**(11-1): p. 693-703.
16. Canham, P.B., *Minimum Energy of Bending as a Possible Explanation of Biconcave Shape of Human Red Blood Cell.* Journal of Theoretical Biology, 1970. **26**(1): p. 61-&.
17. Evans, E.A., *Bending resistance and chemically induced moments in membrane bilayers.* Biophys J, 1974. **14**(12): p. 923-31.
18. Feng, F. and W.S. Klug, *Finite element modeling of lipid bilayer membranes.* Journal of Computational Physics, 2006. **220**(1): p. 394-408.
19. Lorent, J.H., et al., *Plasma membranes are asymmetric in lipid unsaturation, packing and protein shape.* Nature Chemical Biology, 2020. **16**(6): p. 644-+.

20. Doktorova, M., J.L. Symons, and I. Levental, *Structural and functional consequences of reversible lipid asymmetry in living membranes.* Nature Chemical Biology, 2020. **16**(12): p. 1321-1330.
21. Nagle, J.F., *Experimentally determined tilt and bending moduli of single-component lipid bilayers.* Chemistry and Physics of Lipids, 2017. **205**: p. 18-24.
22. Hossein, A. and M. Deserno, *Spontaneous Curvature, Differential Stress, and Bending Modulus of Asymmetric Lipid Membranes.* Biophys J, 2020. **118**(3): p. 624-642.
23. Svetina, S. and B. Zeks, *The Elastic Deformability of Closed Multilayered Membranes Is the Same as That of a Bilayer-Membrane.* European Biophysics Journal with Biophysics Letters, 1992. **21**(4): p. 251-255.
24. Miao, L., et al., *Budding Transitions of Fluid-Bilayer Vesicles - the Effect of Area-Difference Elasticity.* Physical Review E, 1994. **49**(6): p. 5389-5407.
25. Kahraman, O., et al., *Bilayer-thickness-mediated interactions between integral membrane proteins.* Phys Rev E, 2016. **93**: p. 042410.
26. Jensen, M.O. and O.G. Mouritsen, *Lipids do influence protein function - the hydrophobic matching hypothesis revisited.* Biochimica Et Biophysica Acta-Biomembranes, 2004. **1666**(1-2): p. 205-226.
27. Beaven, A.H., et al., *Gramicidin A Channel Formation Induces Local Lipid Redistribution I: Experiment and Simulation.* Biophys J, 2017. **112**(6): p. 1185-1197.
28. Phillips, R., *Physical biology of the cell*. Second edition / ed. 2013, London New York, NY: Garland Science. xxx, 1057 pages.
29. Landau, L.D., et al., *Theory of elasticity*. 3rd English ed. Course of theoretical physics. 1986, Oxford Oxfordshire ; New York: Pergamon Press. viii, 187 p.
30. Hamm, M. and M.M. Kozlov, *Elastic energy of tilt and bending of fluid membranes.* European Physical Journal E, 2000. **3**(4): p. 323-335.
31. Terzi, M.M. and M. Deserno, *Novel tilt-curvature coupling in lipid membranes.* Journal of Chemical Physics, 2017. **147**(8).
32. Pinigin, K.V., et al., *Additional contributions to elastic energy of lipid membranes: Tilt-curvature coupling and curvature gradient.* Phys Rev E, 2020. **102**(4-1): p. 042406.
33. Watson, M.C., et al., *Thermal fluctuations in shape, thickness, and molecular orientation in lipid bilayers.* J Chem Phys, 2011. **135**(24): p. 244701.
34. Ma, L. and W.S. Klug, *Viscous regularization and r-adaptive remeshing for finite element analysis of lipid membrane mechanics.* Journal of Computational Physics, 2008. **227**(11): p. 5816-5835.
35. Seifert, U., *Configurations of fluid membranes and vesicles.* Advances in Physics, 1997. **46**(1): p. 13-137.
36. Miettinen, M.S. and R. Lipowsky, *Bilayer Membranes with Frequent Flip-Flops Have Tensionless Leaflets.* Nano Letters, 2019. **19**(8): p. 5011-5016.
37. Shmakov S, L., *A universal method of solving quartic equations.* Int. J. Pure Appl. Math., 2011. **71**: p. 251-259.
38. Lipowsky, R., *Remodeling of Membrane Shape and Topology by Curvature Elasticity and Membrane Tension.* Advanced Biology, 2022. **6**(1).
39. Nagle, J.F. and S. Tristram-Nagle, *Structure of lipid bilayers.* Biochimica Et Biophysica Acta-Reviews on Biomembranes, 2000. **1469**(3): p. 159-195.

40. Kucerka, N., et al., *Structure of fully hydrated fluid phase DMPC and DLPC lipid bilayers using X-ray scattering from oriented multilamellar arrays and from unilamellar vesicles.* Biophysical Journal, 2005. **88**(4): p. 2626-2637.
41. Venable, R.M., F.L.H. Brown, and R.W. Pastor, *Mechanical properties of lipid bilayers from molecular dynamics simulation.* Chemistry and Physics of Lipids, 2015. **192**: p. 60-74.
42. Kaltenegger, M., et al., *Intrinsic lipid curvatures of mammalian plasma membrane outer leaflet lipids and ceramides.* Biochim Biophys Acta Biomembr, 2021. **1863**(11): p. 183709.
43. Rawicz, W., et al., *Effect of Chain Length and Unsaturation on Elasticity of Lipid Bilayers.* Biophysical Journal, 2000. **79**(1): p. 328-339.
44. Doktorova, M., et al., *A New Computational Method for Membrane Compressibility: Bilayer Mechanical Thickness Revisited.* Biophysical Journal, 2019. **116**(3): p. 487-502.
45. Steinem, C. and M. Meinecke, *ENTH domain-dependent membrane remodelling.* Soft Matter, 2021. **17**(2): p. 233-240.
46. Zeno, W.F., et al., *Synergy between intrinsically disordered domains and structured proteins amplifies membrane curvature sensing.* Nat Commun, 2018. **9**(1): p. 4152.